Materials Horizons

ROYAL SOCIETY OF CHEMISTRY

COMMUNICATION

View Article Online
View Journal | View Issue

Cite this: *Mater. Horiz.*, 2024, **11**, 6361

Received 30th June 2024,
Accepted 23rd September 2024

DOI: 10.1039/d4mh00841c

rsc.li/materials-horizons

A flexible dual-mode sensor with decoupled strain and temperature sensing for smart robots†

Shiying Li,[ab] Mengyu Yang,[ab] Yuanzhao Wu,*[ab] Waqas Asghar,[e] Xingjian Lu,[ab] Haifeng Zhang,[ab] Enhong Cui,[f] Zaojun Fang,[g] Jie Shang,[ab] Yiwei Liu *[ab] and Run-Wei Li *[abcd]

Flexible dual mode strain–temperature sensors that mimic human skin functions are highly desired for wearable devices and intelligent robots. However, integrating dual sensing characteristics into a single sensor for simultaneous and decoupled strain–temperature detection still remains a challenge. Herein, we report a flexible dual-modal sensor that uses a "neutral surface" structural design technique to integrate an independently prepared temperature sensing layer (TSL) and strain sensing layer (SSL), for simultaneous monitoring of strain and temperature, in a decoupled manner. The TSL consists of a PDMS/$BaTiO_3$ based dielectric layer whose dielectric constant and thickness change in response to temperature fluctuations. The SSL consists of a resistive type $Ni_{80}Cr_{20}$ film whose resistance changes in response to external strain. After optimizing the temperature and strain sensing characteristics of the TSL and SSL, the obtained dual-modal flexible sensor has shown a broad temperature sensing range (30 to 200 °C), with high temperature sensitivity (−160.90 fF °C^{-1}), excellent linearity (0.998), and highly discernible temperature resolution (0.1 °C). Additionally, the sensor has also exhibited a wide strain monitoring range (20 to 1000 με), good strain resolution (20 με or 0.002%), and a fast strain response time (54 ms). When practically demonstrated, our sensor has successfully shown independent perception of strain and temperature, which highlights its promising application potential in the fields of smart robotics and intelligent prosthetics.

New concepts

This paper proposes to use the neutral layer for structural design to achieve accurate isolation of strain and temperature stimuli, fabricate a flexible dual-modal temperature strain sensor with a high temperature range, a low detection limit and good decoupling ability, and realize the application demonstration in the tactile perception of intelligent robots. At present, the fabrication of bimodal flexible sensors for temperature and strain has been widely studied, and one way is to realize the simultaneous sensing of temperature and strain by developing materials that respond to both temperature and strain. The above methods have certain advantages in terms of sensor integration, but there are challenges of decoupling. Another approach is to decouple the signal through structural design and material selection, and temperature and strain sensing unit integration. The current research focuses on the wearable environment of the human body, and the temperature of use is near the body temperature of the human body. Based on this, a flexible temperature–strain multifunctional sensor was prepared in this work, which has a high temperature range (30–200 °C), a low detection limit (temperature: 0.1 °C, strain: 0.002%) and good decoupling ability. This innovation provides a new method for the fabrication of flexible dual-modal sensors, highlighting its great application potential in the field of tactile perception in intelligent robots.

Introduction

Flexible sensors having multi-modal sensing functions (pressure, strain, temperature, *etc.*) are widely used in robotics, medical healthcare and other fields.[1–6] A single-modal sensor can accurately perceive a single parameter such as strain[7–9] and

[a] *CAS Key Laboratory of Magnetic Materials and Devices, Ningbo Institute of Materials Technology and Engineering, Chinese Academy of Sciences, Ningbo, 315201, P. R. China. E-mail: wuyz@nimte.ac.cn, liuyw@nimte.ac.cn, runweili@nimte.ac.cn*
[b] *Zhejiang Province Key Laboratory of Magnetic Materials and Application Technology, Ningbo Institute of Materials Technology and Engineering, Chinese Academy of Sciences, Ningbo, 315201, P. R. China*
[c] *School of Future Technology, University of Chinese Academy of Sciences, Beijing 100049, China*
[d] *Center of Materials Science and Optoelectronics Engineering, University of Chinese Academy of Sciences, Beijing 100049, China*
[e] *Mechanical Engineering Department, University of Engineering and Technology Taxila, 47050, Taxila, Pakistan*
[f] *Shandong Aluminum Valley Testing Center, Shandong Aluminum Valley Industrial Technology Institute, Bingzhou, 256200, P. R. China*
[g] *Zhejiang Key Laboratory of Robots and Intelligent Manufacturing Equipment Technology, Ningbo Institute of Materials Technology and Engineering, Chinese Academy of Sciences, Ningbo, 315201, P. R. China*

† Electronic supplementary information (ESI) available. See DOI: https://doi.org/10.1039/d4mh00841c

temperature.[10,11] On the other hand, a dual-modal sensor has the potential to collect two different types of data simultaneously, which improves the accuracy of environmental perception and enables robots to work more effectively in complex external environments. Such multimodal sensing devices when outfitted on robots save space for installation and lower the hardware cost. Temperature and strain are two important parameters that ensure the normal operation of the robots. For example, industrial robots are required to monitor environmental changes (temperature and strain) in real time and achieve precise control. Or they can be used in intelligent prosthetics to achieve humanoid sensing functions (sensing temperature and controlling the range of movement).[12,13] Therefore, it is very crucial to develop such bimodal temperature–strain sensors that can accurately detect minute deformations ($<0.005\%$) and also withstand high temperatures, at the same time. This not only enhances the perception ability of robots but also enables them to perform high-precision tasks more effectively.

At present, two main approaches are used to fabricate bimodal strain–temperature sensors. In the first approach, such materials are developed that are responsive to both temperature and strain, enabling simultaneous sensing of both parameters.[14–17] Examples of these materials include some composites made from silver nanowires,[18] graphite,[19] ionic liquids,[20] carbon nanotubes,[21,22] *etc.* For instance, Chhetry *et al.* developed a strain–temperature bimodal sensor, which demonstrated a TCR of 0.1736% $^{\circ}C^{-1}$ and a low detection limit of 0.023% within the 25–50 °C temperature range, by taking advantage of the temperature-sensitive properties and microcrack propagation mechanism of allylamine and BP nanosheets.[23] Li *et al.* developed a multi-walled carbon nanotube/polydimethylsiloxane (MWNTs/PDMS) based material that exhibited excellent resistance changes over a tensile range of 0% to 120%, with a linear temperature correlation of 0.998 between 0 °C and 100 °C. They integrated their sensor into smart gloves to successfully achieve gesture and temperature recognition.[21] The abovementioned sensors/materials can accurately detect both strain and temperature stimuli but are unable to decouple both stimuli.

In the second approach, separately prepared temperature and strain sensing units are integrated together, which can effectively reduce the problem of signal crosstalk.[24–26] For example, Chen *et al.* prepared a core–shell structure of conductive hydrogel/thermochromic elastomeric fibers to detect strain and temperature.[27] The change in the resistance of the strain sensor and the change in the color of the temperature sensor ensured that the signals of two adjacent sensors do not interfere with each other. Similarly, Xu *et al.* prepared a multimodal strain–temperature sensor and achieved temperature sensing by introducing a reversible thermochromic ink.[28] The principles of capacitance, thermochromism, and triboelectricity are used to simultaneously sense and distinguish between strain, temperature, and pressure excitation. In our previous research work, we employed magnetic amorphous fibers and decoupled strain (minimum 0.05%) and temperature (minimum 0.1 °C) signals by using the magnetoelastic effect and thermoelectric effect of tubular heterogeneous coils.[29] Jung *et al.* designed a multi-modal sensor for pressure, temperature, and flow measurements by arranging the sensors vertically and realized pressure sensing in the range of 600 Pa–600 kPa and temperature sensing in the range of 50–150 °C.[30] Despite the progress achieved to date, the development of such a flexible dual modal temperature–strain sensor still remains a major challenge, which can exhibit a wide temperature sensing range (above 150 °C), a low strain detection limit and decoupling capability to fulfill the needs of robots working in extreme environments (as shown in Table 1).

Herein, we demonstrate a flexible dual-modality sensor that can simultaneously sense and decouple the stimuli of temperature and strain. The dielectric layer of the capacitive temperature sensing unit (TSL) is made of PDMS/$BaTiO_3$, which changes its dielectric constant and thickness in response to external temperature changes. The $Ni_{80}Cr_{20}$ film serves as the resistive SSL, whose resistance varies with the applied strain. The ''neutral surface'' structural design is used to successfully decouple strain and temperature sensing. The strain, temperature, and resistance correlation equations are established to decouple strain. After optimizing the temperature and strain sensing parameters of TSL and SSL, a strain–temperature dual-mode flexible sensor is obtained, which exhibits a broad temperature sensing range (30–200 °C), with excellent linearity (0.998), ultra-high temperature sensitivity (−160.90 fF $^{\circ}C^{-1}$), and highly discernible temperature resolution (0.1 °C). Additionally, the sensor has also shown a wide strain monitoring range (20–1000 με), good strain resolution (20 με or 0.002%),

Table 1 Comparison table of strain–temperature dual mode sensors

Material	Maximum temperature	Strain detection limit	Strain-GF	Temperature detection limit	Temperature sensitivity	Decoupling	Ref.
IL	80	0.001	0.824	0.5	0.0094	No	20
PANI	110	0.05	18.28	2.7	0.016	No	17
NP/CNC/Co	100	5×10^{-4}	5.29	0.1	54.49 μV	Yes	29
LiBr	97	0.001	5.25	—	0.00254	No	31
rGo	55	0.003	—	—	Color reflection	Yes	27
LiCl	80	0.01	17.3	0.2	5.51	No	32
AgNW/CNF	97	0.002	34.06	—	2600	No	18
MAPT	40	—	1933.3	0.2	25.3 μV	Yes	33
BTO/PDMS/$Ni_{80}Cr_{20}$	200	2×10^{-4}	2.161	0.1	−160.90 fF	Yes	This work

and a fast response time (54 ms). Finally, when the sensor is integrated into the gripper of a robot for practical demonstration, our sensor has successfully shown independent perception of strain and temperature, which highlights its application potential in the fields of smart robotics and intelligent prosthetics.

Experimental section

Materials

Barium titanate ($BaTiO_3$) is an outstanding dielectric material for capacitive sensors, whose dielectric constant lies in the range of 4000–5000. It also serves as a thermosensitive material, as its dielectric constant decreases with temperature rise, making it ideal for temperature sensors.[34] Besides this, NiCr thin films offer several advantages, including high resistivity, a low temperature coefficient of resistance, and high strain sensitivity.[35,36] Importantly, these films are capable of functioning at temperatures as high as 400 °C. For example, Kazi *et al.* used NiCr as a strain-sensitive material and achieved a stable and low resistance temperature coefficient with favourable strain sensitivity.[37] By keeping in mind the abovementioned properties, $BaTiO_3$ and $Ni_{80}Cr_{20}$ were selected to develop temperature and strain sensing materials, respectively.

Preparation of the temperature sensing layer (TSL)

To prepare a capacitive type TSL, $BaTiO_3$ nanoparticles were dispersed in PDMS elastomer (in various weight ratios ranging from 33.3% to 66.7%), followed by magnetically stirring and degassing the mixture for 20 minutes. Afterwards, the mixture was spin-coated onto a silicon wafer to form a PDMS@$BaTiO_3$ thin film. Finally, LM electrodes were coated on both sides of the thin film to complete the formation of the TSL.

Preparation of the strain sensing layer (SSL)

The SSL was obtained by depositing the strain gauge shaped $Ni_{80}Cr_{20}$ thin film on a PI substrate (33 mm × 33 mm × 0.125 mm) by using a strain gauge mask (6 mm × 3 mm) and a DC magnetron sputtering system. The DC magnetron sputtering system had a 51 mm target diameter and a base pressure range of 5×10^{-5} Pa. The Pt thin film was also patterned using the DC magnetron sputtering system to prevent oxidation of the $Ni_{80}Cr_{20}$ thin film.

Characterization of temperature and strain sensing performance

The capacitance variations of the sensor were measured by using an impedance analyzer (IM 3570, HIOKI). Precise temperature control was achieved by using a KSL-1100 box furnace. The weight loss of PDMS@$BaTiO_3$ film was investigated by employing a thermal weight loss instrument (TGA2019F1) under a nitrogen atmosphere. A nanovoltmeter device (Agilent 34420A) and a current source (KEITHLEY 6221) were used in combination with the 4-terminal method to characterize the electrical performance of the thin film samples. A universal material testing machine (Instron 5943) was used to apply the strain on test samples, while a strain gauge (ST-3C) was employed to monitor the applied strain magnitude, in real time. At high temperature, the sensing element was secured by using a self-made thin film fixture. Deformation was applied to the sensing element by adjusting the knobs on the fixture. The deformation test of the knee joint of the robot at high temperature was carried out by using a walk-in high and low temperature damp heat test chamber (ESPEC, SEWTH-A-100LH, Japan).

Results and discussion

Sensing principle and preparation process of the dual mode flexible sensor

The structure and preparation technique of our flexible dual-mode temperature–strain sensor are shown in Fig. 1. The main components of the sensor include a temperature sensing layer (TSL), a strain sensing layer (SSL), electrode layers, and an encapsulation layer (Fig. 1a). A capacitive-type temperature sensor is prepared by coating liquid metal (LM) electrodes on both sides of the PDMS/$BaTiO_3$ thin film. Temperature variations affect the dielectric constant and the thickness of the TSL which ultimately leads to variations in the capacitance of the temperature sensor. The resistance of serpentine shaped SSL changes on application of bending strain. Fig. 1b and c shows the real-time capacitance and resistance variations of our dual-mode sensor in conjunction with decoupling analysis when temperature and strain changes occur. The temperature is calculated using eqn (1):

$$C = \frac{\varepsilon_0 \cdot (32.7 - 0.09625T) \cdot w \cdot l}{d^0_{\mathrm{PDMS/BTO}} \cdot \left(1 + \frac{\gamma_{\mathrm{PDMS/BTO}}}{3} T\right)} \quad (1)$$

where C is the capacitance of the sensor; T is the temperature; ε_0 is the dielectric constant of the TSL; $\gamma_{\mathrm{PDMS/BTO(T)}}$ is the volume expansion coefficient of the TSL; $d^0{}_{\mathrm{PDMS/BTO}}$ is the initial thickness of the TSL; and l and w are the length and width of the electrode. The mathematical proof of eqn (1) is shown in the ESI.†

A resistive type SSL is developed by utilizing a strain gauge shaped $Ni_{80}Cr_{20}$ thin film, whose resistance changes in response to external deformations. When considering the effects of both strain (E_s) and temperature (T), the measured strain can be calculated using eqn (2):

$$R(T,E_s) = R_0 + (R_0 \times \mathrm{GF} \times E_s) + (R_0 \times \mathrm{TCR} \times T) \quad (2)$$

where R and R_0 represent the sensor resistances in stretched and initial states, E_s denotes the strain acting on the sensor, GF is the strain sensitivity or gage factor and TCR is the temperature coefficient of resistance. The mathematical derivation of eqn (2) is provided in the ESI.† Finally, the TSL with the electrode layer is encapsulated by positioning the PI film as the bottom layer and the SSL as the top layer.

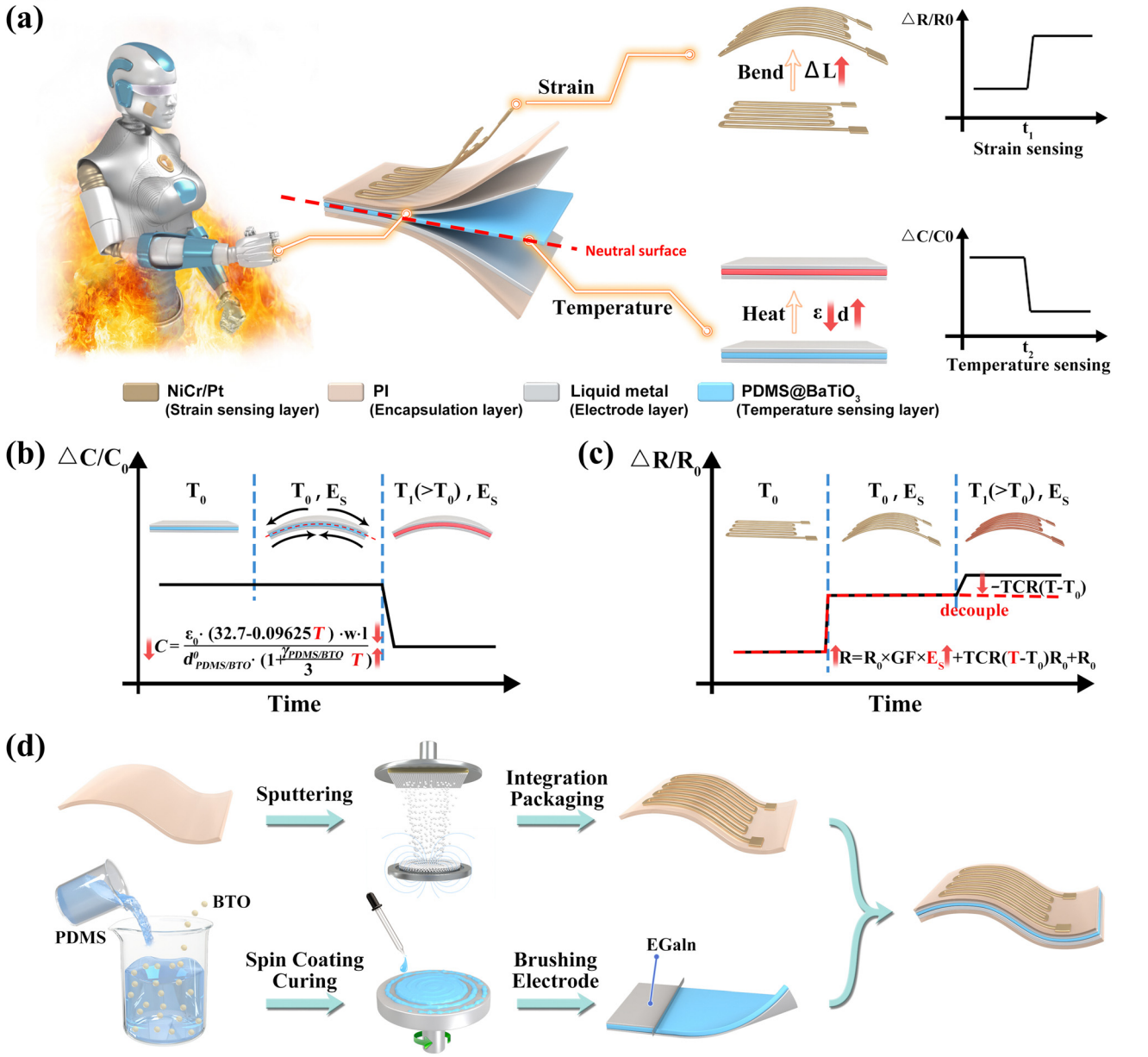

Fig. 1 Structure and preparation technique of the dual mode strain–temperature sensor. (a) Schematic diagram showing the components of our sensor, which include a capacitive temperature sensing layer (TSL), a resistive type strain sensing layer (SSL), an electrode layer, and an encapsulation layer; (b) the sensing principle of the TSL of our dual modal sensor; (c) the sensing principle of the SSL of our dual modal sensor; (d) schematic diagram showing the detailed preparation process of our dual modal strain–temperature sensor.

Fig. 1d shows the detailed preparation process of the flexible dual mode temperature–strain sensor. Initially, $BaTiO_3$ and PDMS are mixed in different proportions, followed by stirring the solution for 20 minutes. Subsequently, the solution is spin-coated onto a silicon wafer, followed by curing the coated wafer at 70 °C for 2 hours. This yields a temperature-sensitive PDMS/$BaTiO_3$ thin film. Then LM (EGaIn) is coated on both sides of the thin film to serve as electrodes. In addition, the SSL is obtained by depositing $Ni_{80}Cr_{20}$ thin film on a PI substrate by using a strain gauge mask and a DC magnetron sputtering system. The final sensor assembly is obtained by placing the TSL between the PI film (bottom layer) and the SSL (top layer).

Optimization of temperature sensing performance

To investigate the effect of TSL thickness on temperature sensing performance, variable thickness TSL layers are prepared by adjusting spin-coating speeds at 600, 800, 1000, and 1200 rpm, respectively. Based on the SEM images of TSL cross-section, we obtained the following TSL thickness values, *i.e.* 163 μm, 138 μm, 105 μm, and 78 μm, respectively (Fig. S1, ESI†). Fig. S2 (ESI†) confirms that humidity affects the capacitance of

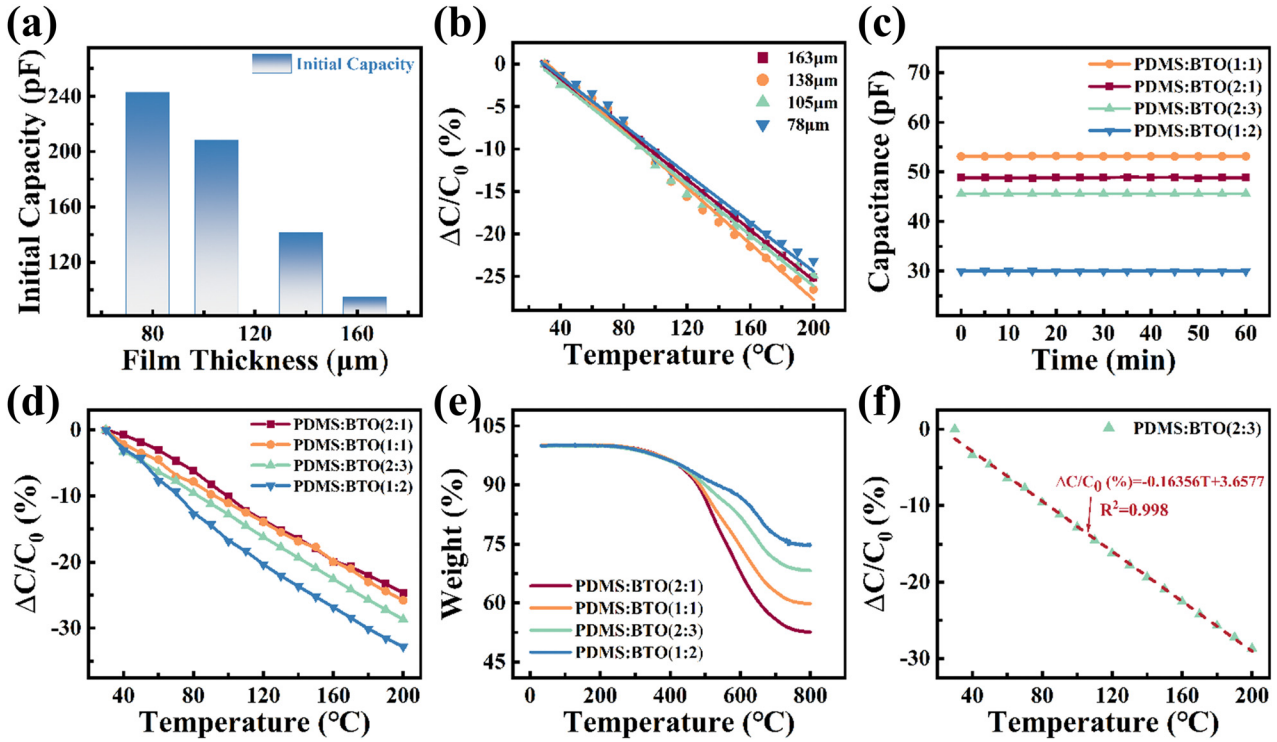

Fig. 2 Optimization of the temperature sensing performance of the TSL. (a) Variation in the initial capacitance of the TSL with different film thicknesses; (b) $\Delta C/C_0$ *vs.* temperature curves of the TSL at different thicknesses; (c) the initial capacitance and stability of the temperature sensor at different mass ratios; (d) $\Delta C/C_0$ *vs.* temperature curves of the TSL at different mass ratios; (e) thermogravimetric curves of the TSL at different doping ratios; (f) $\Delta C/C_0$ *vs.* temperature curve of the TSL showing a good linear relationship between ΔT and $\Delta C/C_0$ in the temperature range from 30 °C to 200 °C. The slope of the curve is −0.16356.

the TSL, that is why we encapsulated our TSL in a waterproof membrane to reduce the effect of humidity. Fig. 2a shows that the thickness of the TSL has a significant impact on the initial capacitance. As the thickness increases from 78 μm to 163 μm (with an electrode size of 15 × 15 mm^2), the initial capacitance of the TSL decreases from 242.8 pF to 94.5 pF, which is consistent with eqn (1). We have also studied the effect of TSL thickness on the temperature response of the TSL. Fig. 2b shows that $\Delta C/C_0$ changes from 23% to 25% at 200 °C when TSL thickness varies from 78 μm to 163 μm. Also, the slope of the relative capacitance curves of the TSL remains almost unaltered with increasing thickness.

We have also investigated the influence of $BaTiO_3$ content on the dielectric constant of the capacitor, along with the impact of the PDMS : $BaTiO_3$ mass ratio on the initial capacitance (Fig. 2c). When the mass ratio of PDMS : $BaTiO_3$ increases from 2 : 1 to 1 : 2, the initial capacitance rises and then decreases (the maximum value of initial capacitance is attained at a 1 : 1 mass ratio). The increase in $BaTiO_3$ content during the preparation process leads to an increase in the dielectric constant, while the density of the mixed solution also increases, resulting in a thicker film at the same spin-coating speed. The initial capacitance decreases when the thickness effect exceeds the change in the dielectric constant.

Fig. 2d illustrates the capacitance–temperature profiles of TSLs with various mass ratios, revealing a negative correlation between the temperature and capacitance of the TSL. Additionally, the capacitance of the TSL gradually reduces as the temperature increases from 40 °C to 200 °C. As the $BaTiO_3$ content increases, the capacitance change amplitude also increases, and the temperature sensitivity reaches its maximum value at a 1 : 2 mass ratio. To assess the stability of TSLs at various temperatures, thermogravimetric analysis (TGA) was performed on samples with different weight ratios. As shown in Fig. 2e and Fig. S3 (ESI†), the mass loss of the TSL occurs at approximately 250 °C. With an increase in the $BaTiO_3$ w/w ratio, the mass loss rate progressively slows down. This phenomenon is attributed to the $BaTiO_3$ addition, which creates a heat conduction pathway, resulting in an increase in thermal conductivity and a decrease in the rate of weight loss. Considering the uniformity of $BaTiO_3$ dispersion in the film (Fig. S4, ESI†) and its thermal stability, a mass ratio of 2 : 3 was chosen as the optimal mixing ratio.

Furthermore, the $\Delta C/C_0$ of the TSL (2 : 3) decreases as the temperature increases from 40 to 200 °C (Fig. 2f). This phenomenon can be attributed to the temperature-induced fall in the dielectric constant, as well as the increase in medium thickness caused by the volume expansion of the medium, which eventually results in a decrease in capacitance as the temperature increases. The TCC value (−163.56% $°C^{-1}$, R^2 = 0.998) and sensitivity (160.90 fF $°C^{-1}$) of our sensor exceed those of many other previously reported temperature sensors

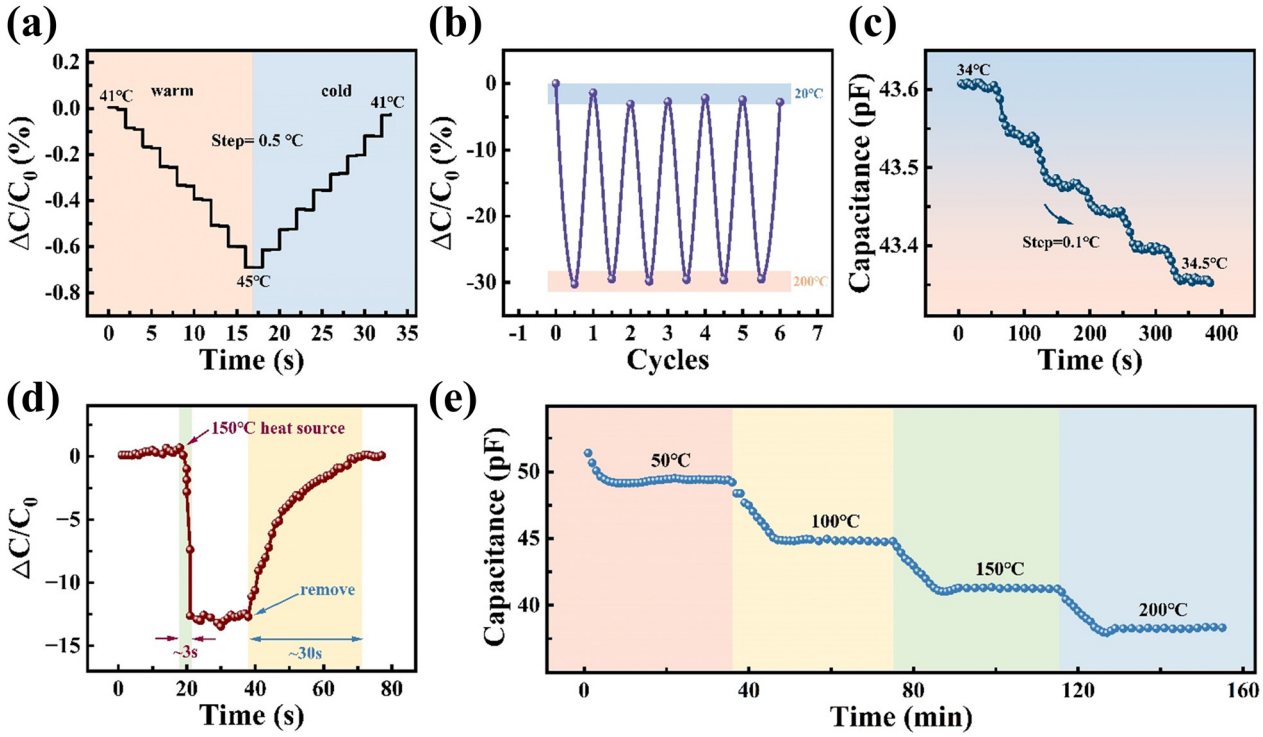

Fig. 3 Temperature sensing performance of the TSL. (a) Dynamic response of the TSL obtained by heating it up and cooling down between 41 °C and 45 °C; (b) a graph showing the thermal cycling stability of our TSL; (c) capability of our TSL to successfully detect the minimum temperature of 0.1 °C; (d) response time evaluation of our TSL, with green and yellow areas indicating the response and relaxation times, respectively; (e) the capacitance of the TSL at different temperatures showing its excellent stability.

prepared by using reduced graphene oxide, Au, and polysilicon as heat-sensitive materials (Table S1, ESI†).[38–43]

To investigate the dynamic response, we gradually heated the TSL from 41 °C to 45 °C and then cooled it back to 41 °C (at an interval of 0.5 °C). As it is obvious from Fig. 3a, the capacitance of the TSL changes accordingly with the gradual variation of temperature, which confirms the good dynamic stability of our TSL. Fig. 3b confirms the excellent cycling stability of the TSL over a wide temperature range of 20 °C to 200 °C. Our TSL can successfully detect the minimum temperature of 0.1 °C (Fig. 3c) and has demonstrated a response time of 3s when it is exposed to a heat source at 150 °C (Fig. 3d). Fig. S5 (ESI†) illustrates that the dielectric constant of the TSL changes gradually when a sudden temperature drop occurs from 150 °C to 5 °C (*i.e.* variation of 145 °C). It takes about 30 seconds for the TSL to stabilize (Fig. 3d) on a gradual temperature drop from 150 °C to 25 °C and it will be automatically more than 30 s on a sudden temperature drop from 150 °C to 5 °C (Fig. S5, ESI†). Undoubtedly, the response time of the TSL will be significantly lower (to a matter of milliseconds), if TSL performance is evaluated for smaller temperature variations. To further confirm the operational stability of the TSL, we stabilized our TSL at 50 °C, 100 °C, 150 °C, and 200 °C for 30 minutes and then recorded the capacitance change of the TSL at each temperature. Fig. 3e verifies that the capacitance of the TSL capacitor shows very little fluctuations at a fixed temperature, which confirms the excellent stability and long-term sensing performance of our TSL. When compared with previously reported capacitive temperature sensors (Table S1, ESI†),[38–43] our TSL exhibits superior performance in terms of temperature sensitivity and the operating range.

Optimization of strain sensing performance

The $Ni_{80}Cr_{20}$ thin film was prepared by magnetron sputtering to serve as a resistive flexible strain sensor. Initially, the effects of different growth processes on the resistivity and temperature coefficient of resistance (TCR) of $Ni_{80}Cr_{20}$ films were studied. Fig. S6 (ESI†) shows the atomic force microscopy (AFM) images of $Ni_{80}Cr_{20}$ thin film, obtained at different sputtering powers. At sputtering powers of 50 W, 70 W, 90 W, 110 W, and 130 W, the corresponding roughness values obtained are 0.978, 1.43, 2.05, 2.49, and 2.97 nm, respectively. Moreover, Fig. S7 (ESI†) shows the $\Delta R/R$ of the sample with temperature at different powers, and the SSL resistivity as a function of the sputtering power of the $Ni_{80}Cr_{20}$ film. Table S2 (ESI†) confirms that the resistivity of the thin film increases with the increase of sputtering power. This occurs because increasing sputtering power leads to more film defects and roughness, which in turn increases the resistivity of the film.

Fig. S8 (ESI†) illustrates the correlation between the TCR and sputtering power of the flexible strain sensing unit which confirms that the TCR increases when the sputtering power increases from 596 ppm $°C^{-1}$ at 50 W to 1926 ppm $°C^{-1}$ at 130 W. This is attributed to the higher sputtering power

resulting in more defects and a less dense structure in the $Ni_{80}Cr_{20}$ thin film, which ultimately increases the TCR of the film. Therefore, we selected a sputtering power of 50 W for further analysis. We also investigated the impact of sputtering air pressure on the resistivity and TCR of $Ni_{80}Cr_{20}$ films (Fig. S8, ESI†). It is found that increasing sputtering pressure also increases the TCR, which occurs because sputtering air pressure exhibits a direct relation with defects and roughness of the film. Fig. S9 (ESI†) shows the obtained roughness values of 0.904, 0.978, 1.21, 1.64, 2.03 and 2.44 nm at various sputtering pressures of 0.4, 0.5, 0.6, 0.7, 0.8 and 0.9 Pa, respectively. Fig. S10 (ESI†) shows the $\Delta R/R$ of the sample with temperature at different air pressures, and the SSL resistivity as a function of sputtering air pressure of $Ni_{80}Cr_{20}$ film. Table S3 (ESI†) confirms that the resistivity of the thin film increases with the increase of sputtering pressure. The thin film deposited at lower sputtering pressure exhibits fewer defects and less surface roughness because of its more dense structure. As a result, the optimal sputtering pressure value obtained is 0.4 Pa.

Furthermore, we also studied the strain sensing performance of the SSL. Fig. 4a shows the $\Delta R/R$ of the $Ni_{80}Cr_{20}$ film at 25, 100, 150 and 200 °C as a function of strain. It is evident from the graph that the $\Delta R/R$ of the SSL increases linearly with the applied strain and the sensitivities obtained are 1.648, 1.846, 1.936 and 2.161, respectively. On application of repeated strain (Fig. 4b), the resistance of the SSL changes steadily which confirms the excellent dynamic stability of our SSL. To calculate the limit of detection (LOD), we applied a minute strain of 20 με (0.002%) on the SSL and it successfully detected such a minute strain by showing a resistance change of 25 ppm (Fig. 4c). So our SSL exhibits a LOD of 20 με, which exceeds the LOD for previously reported microstructured sensors (Table S4, ESI†).[44–50] The response time of the sensor is evaluated by applying 1000 με to the SSL, as shown in Fig. 4d. Our sensor has demonstrated a loading and an unloading response time of 54 ms and 74 ms, respectively. Fig. 4e shows the excellent repeatability of the SSL, as the resistance signal keeps its waveform between 0 and 1000 cycles.

Sensor electrical response to temperature and strain

After temperature and strain sensing optimization, both the SSL and TSL are integrated to obtain a dual mode strain–temperature flexible sensor. Fig. 5 demonstrates the capability of our sensor to decouple strain and temperature sensing. Initially, we studied the effect of externally applied bending strain on the capacitance of our sensor. When the sensor is bent from 20 mm to 8 mm (Fig. 5a), its capacitance changes slightly due to variations in the geometry of the sensor. More interestingly, when the thickness of the TSL dielectric layer is kept at 140 μm, the capacitance of the sensor changes only by 1.57% (Fig. S11, ESI†). This occurs because the dielectric layer is located exactly on the neutral surface of the sensor at a thickness of 142 μm, which limits its deformation during tension and compression and thus isolates the effect of strain

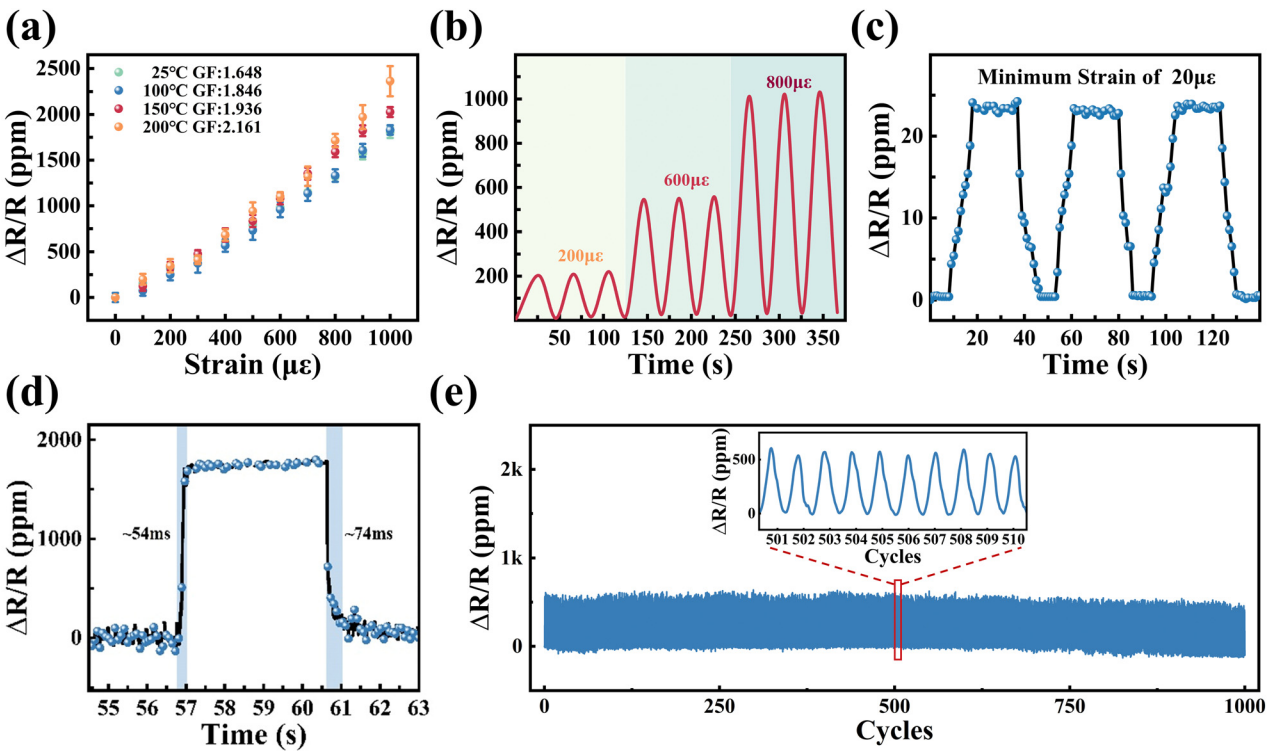

Fig. 4 Optimization of strain sensing performance. (a) Strain sensitivities of the SSL at different temperatures; (b) response curves of the SSL under the application of repeated strain; (c) a graph showing the LOD of our SSL; (d) response time evaluation of the SSL; (e) response of the SSL to cyclic loading indicating its excellent repeatability.

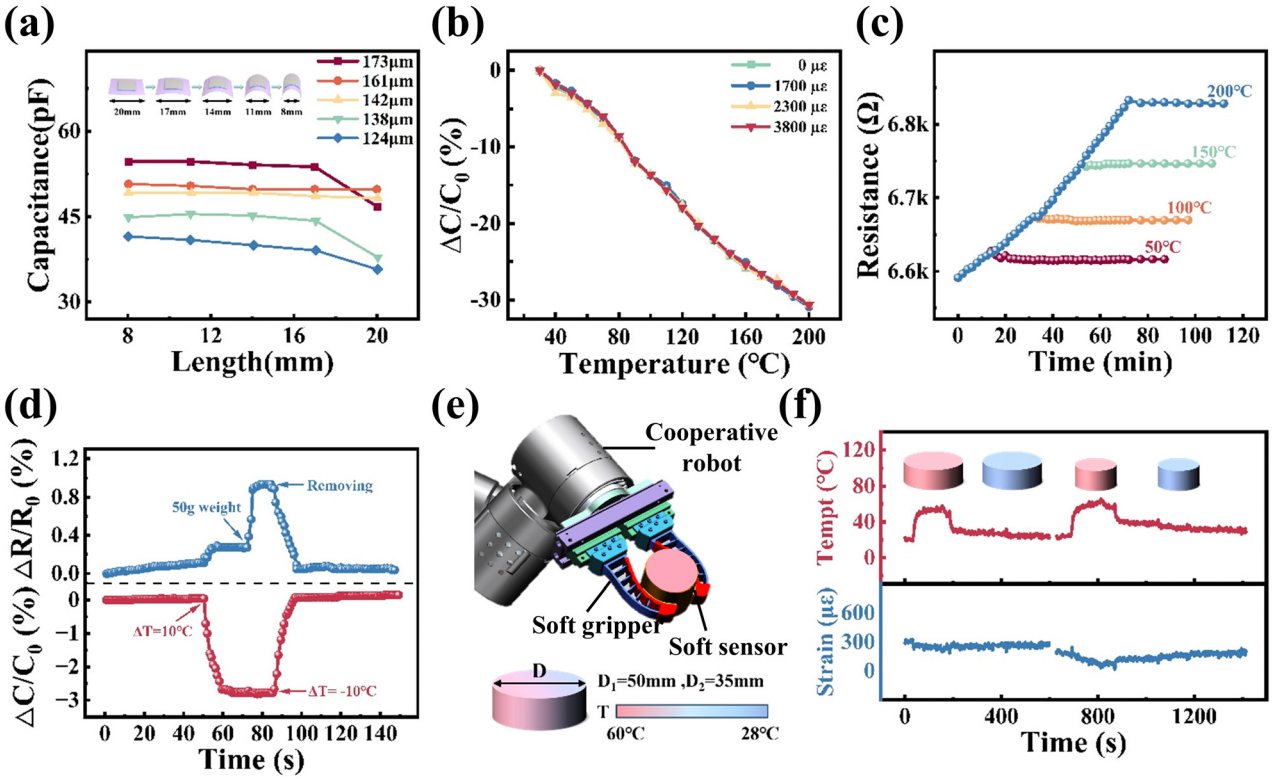

Fig. 5 Characteristics of temperature–strain bimodal sensors in response to thermal and mechanical stimuli; (a) effect of film thickness on the capacitance of our sensor during bending; (b) $\Delta C/C_0$ *vs.* temperature curves of our sensor under various bending strains; (c) resistance variation of the NiCr thin film based strain sensor with heating time and holding time; (d) real-time monitoring of temperature and strain under various conditions; (e) bimodal sensor incorporated soft gripper to attain strain and temperature detection during the grasping operation; (f) the real-time output of the temperature of cylinders and the strain of the soft gripper, obtained when the dual-modal sensor incorporated soft gripper is used to grasp various cylinders.

on the capacitance.[51] Fig. 5b depicts the sensor capacitance as a function of temperature and applied strain. It is evident that the $\Delta C/C_0$ of the sensor decreases independently of the increase of temperature, even under various applied strains, which confirms that our sensor can effectively isolate the influence of strain on temperature monitoring. At 200 °C, the sensor's $\Delta C/C_0$ reaches 32.83%, which is much higher than the previously discussed strain-induced capacitance change (1.57%). The interference of temperature on strain monitoring is further studied by keeping our sensor at 50 °C, 100 °C, 150 °C and 200 °C for 40 min (Fig. 5c). When the temperature is kept stable, the resistance signal remains almost straight and mainly comes from applied strain (at that moment), which validates the decoupling strain and temperature sensing capabilities of our sensor.

To simultaneously apply both strain and temperature, we placed our sensor at an initial temperature of 190 °C by setting its initial resistance and initial capacitance (Fig. 5d). When the temperature increases to 200 °C, the capacitance decreases by 2.9%, while the resistance increases by 0.279%. Afterwards, when a weight of 50 g is applied at a temperature of 200 °C, the resistance of the sensor changes by 0.87%, while the capacitance remains relatively stable. Finally, when the weight is reduced and the temperature is also gradually reduced to its initial value of 190 °C, the resistance and capacitance return to their initial states. This confirms that our sensor is highly effective in distinguishing between temperature and strain stimuli. To simulate the grasping operation of a human hand (Fig. 5e), we placed our sensor on the flexible soft gripper of the robot, to grasp both small and large cylinders. The gripper grasped the larger cylinder from hot (~56 °C) to cool (~23 °C) and the smaller cylinder from hot (~65 °C) to cool (~28 °C), sequentially (Fig. S12, ESI†). The resultant capacitance and resistance variations of the sensor are shown in Fig. S13 (ESI†), which confirms that our sensor is fully capable of independently monitoring temperature and strain. Fig. 5f depicts the real-time temperature and strain magnitude variations occurred during the grasping process, as obtained by using eqn (1) and (2). Finally, to confirm the accuracy of robot posture detection in high temperature environments, we measured the knee flexion angle of the robot at 30 °C and 80 °C, by using an environmental chamber (Fig. S14, ESI†). Fig. S15 (ESI†) confirms that our sensor successfully detects the ambient temperature and removes the effect of temperature on strain monitoring, using our proposed decoupling formula. The successful detection of the size and temperature of the grasped object and effective monitoring of the robot's movement in high-temperature environments highlights the great

application potential of our sensor in diverse fields, including intelligent robots, search and rescue in challenging environments, and advanced medical equipment.

Conclusion

In summary, we demonstrate a simple and cost-effective methodology for developing a flexible dual-modal sensor that measures both temperature and strain. This sensor integrates a PDMS/$BaTiO_3$-based thermal material with a $Ni_{80}Cr_{20}$-based strain sensing component. The ''neutral surface'' structure is designed to isolate the strain measurement and ensure temperature independence. Correlation equations are established for strain, temperature, and resistance, effectively decoupling strain from ambient temperature variations. After optimization of the temperature and strain sensing functionalities, the sensors demonstrate superior performance across a broad temperature range (30–200 °C). This enhancement is attributed to simultaneous changes in the dielectric constant and volume of the PDMS/$BaTiO_3$ composites in response to temperature fluctuations, resulting in exceptional sensitivity (-160.90 fF $°C^{-1}$), outstanding linearity (0.998), and precise temperature resolution (0.1 °C). Additionally, due to its excellent thermal stability at high temperatures (200 °C) and the substantial initial resistance of the $Ni_{80}Cr_{20}$-based strain grid, the sensor offers an extensive strain monitoring range (20–1000 με), with a minimum detectable strain of 20 με (0.002%) and a rapid strain response time of 54 ms. Leveraging its advanced temperature–strain discrimination capabilities, the intelligent robot gripper mimics human-like perceptions, enabling accurate identification of object dimensions and temperature states. This highlights the significant potential applications of our sensors in the field of intelligent robotics. Moreover, further research should be done to further improve the stretchability and response time of the current sensor. Besides this, the influence of humidity should also be studied along with temperature–strain stimuli to realize futuristic multimodal sensing devices.

Author contributions

S. Y. Li: formal analysis, data curation, writing, investigation; M. Y. Yang: methodology, visualization, investigation, resources; Y. Z. Wu: writing – original draft, review & editing, supervision; W. A.: writing – review & editing, validation; X. J. Lu: writing – original draft, data curation; H. F. Zhang: visualization, investigation; E. H. Cui: formal analysis; Z. J. Fang: visualization; J. S.: data curation, supervision; Y. W. Liu: methodology, review & editing, supervision; R. W. Li: formal analysis, supervision, validation.

Data availability

The data that support the findings of this study are available from the corresponding author upon reasonable request.

Conflicts of interest

The authors declare no competing interests.

Acknowledgements

This research was partially supported by the National Key R&D Program of China (2023YFC3603501), the National Natural Science Foundation of China (62174165, 51931011, U20A6001, 52127803, U22A2075, M-0152, U22A20248, 52201236, 62204246, and 52301256), the Outstanding member of the Youth Innovation Promotion Association of the Chinese Academy of Sciences (Y2022080), the ''Pioneer'' and ''Leading Goose'' R&D Program of Zhejiang (2022C01032), the Zhejiang Province project (2022R52004), the Natural Science Foundation of Zhejiang Province (LD22E010002), the Ningbo Natural Science Foundations (20221JCGY010312), the Ningbo Key Research and Development Program (2023Z097, 2024Z143, and 2024Z148), and the Ningbo Public Welfare Program (2023S067).

Notes and references

1 M. Amjadi, K.-U. Kyung, I. Park and M. Sitti, *Adv. Funct. Mater.*, 2016, **26**, 1678–1698.
2 Y. Dong, L. Wang, N. Xia, Z. Yang, C. Zhang, C. Pan, D. Jin, J. Zhang, C. Majidi and L. Zhang, *Sci. Adv.*, 2022, **8**, eabn8932.
3 Z. H. Guo, Z. Zhang, K. An, T. He, Z. Sun, X. Pu and C. Lee, *Research*, 2023, **6**, 0154.
4 J. Escobar-Naranjo, G. Caiza, P. Ayala, E. Jordan, C. A. Garcia and M. V. Garcia, *Appl. Sci.*, 2023, **13**, 7202.
5 A. Kotikian, C. McMahan, E. C. Davidson, J. M. Muhammad, R. D. Weeks, C. Daraio and J. A. Lewis, *Sci. Robot.*, 2019, **4**, eaax7044.
6 K. Hussain, X. Wang, Z. Omar, M. Elnour and Y. Ming, in 2021 *International Conference on Computer, Control and Robotics (ICCCR)*, IEEE, Shanghai, China, 2021, 66–69.
7 S. Li, G. Liu, R. Li, Q. Li, Y. Zhao, M. Huang, M. Zhang, S. Yin, Y. Zhou, H. Tang, L. Wang, G. Fang and Y. Su, *ACS Nano*, 2022, **16**, 541–553.
8 G. Yang, X. Tang, G. Zhao, Y. Li, C. Ma, X. Zhuang and J. Yan, *Chem. Eng. J.*, 2022, **435**, 135004.
9 P. Zhan, Y. Jia, W. Zhai, G. Zheng, K. Dai, C. Liu and C. Shen, *Composites, Part A*, 2023, **167**, 107431.
10 X. Ren, K. Pei, B. Peng, Z. Zhang, Z. Wang, X. Wang and P. K. L. Chan, *Adv. Mater.*, 2016, **28**, 4832–4838.
11 G. Liu, Q. Tan, H. Kou, L. Zhang, J. Wang, W. Lv, H. Dong and J. Xiong, *Sensors*, 2018, **18**, 1400.
12 Y. Wu, Y. Liu, Y. Zhou, Q. Man, C. Hu, W. Asghar, F. Li, Z. Yu, J. Shang, G. Liu, M. Liao and R.-W. Li, *Sci. Robot.*, 2018, **3**, eaat0429.
13 C. Wu, T. W. Kim, J. H. Park, B. Koo, S. Sung, J. Shao, C. Zhang and Z. L. Wang, *ACS Nano*, 2020, **14**, 1390–1398.
14 J. Gu, J. Huang, G. Chen, L. Hou, J. Zhang, X. Zhang, X. Yang, L. Guan, X. Jiang and H. Liu, *ACS Appl. Mater. Interfaces*, 2020, **12**, 40815–40827.

15 S. Pradhan and V. K. Yadavalli, *ACS Appl. Electron. Mater.*, 2021, **3**, 21–29.
16 L. Ji, L. Yan, M. Chao, M. Li, J. Gu, M. Lei, Y. Zhang, X. Wang, J. Xia, T. Chen, Y. Nie and T. Chen, *Small*, 2021, **17**, 2007122.
17 G. Ge, Y. Lu, X. Qu, W. Zhao, Y. Ren, W. Wang, Q. Wang, W. Huang and X. Dong, *ACS Nano*, 2020, **14**, 218–228.
18 R. Yin, S. Yang, Q. Li, S. Zhang, H. Liu, J. Han, C. Liu and C. Shen, *Sci. Bull.*, 2020, **65**, 899–908.
19 L. Lu, B. Yang and J. Liu, *Chem. Eng. J.*, 2020, **400**, 125928.
20 N. Jiang, H. Li, D. Hu, Y. Xu, Y. Hu, Y. Zhu, X. Han, G. Zhao, J. Chen, X. Chang, M. Xi and Q. Yuan, *Compos. Commun.*, 2021, **27**, 100845.
21 Y. Li, C. Zheng, S. Liu, L. Huang, T. Fang, J. X. Li, F. Xu and F. Li, *ACS Appl. Mater. Interfaces*, 2020, **12**, 23764–23773.
22 M. Lin, Z. Zheng, L. Yang, M. Luo, L. Fu, B. Lin and C. Xu, *Adv. Mater.*, 2022, **34**, 2107309.
23 A. Chhetry, S. Sharma, S. C. Barman, H. Yoon, S. Ko, C. Park, S. Yoon, H. Kim and J. Y. Park, *Adv. Funct. Mater.*, 2021, **31**, 2007661.
24 G. Y. Bae, J. T. Han, G. Lee, S. Lee, S. W. Kim, S. Park, J. Kwon, S. Jung and K. Cho, *Adv. Mater.*, 2018, **30**, 1803388.
25 M. Jung, K. Kim, B. Kim, H. Cheong, K. Shin, O.-S. Kwon, J.-J. Park and S. Jeon, *ACS Appl. Mater. Interfaces*, 2017, **9**, 26974–26982.
26 Q. Chen, H. Tang, J. Liu, R. Wang, J. Sun, J. Yao, Z. Shao and X. Chen, *Chem. Eng. J.*, 2021, **422**, 130091.
27 J. Chen, H. Wen, G. Zhang, F. Lei, Q. Feng, Y. Liu, X. Cao and H. Dong, *ACS Appl. Mater. Interfaces*, 2020, **12**, 7565–7574.
28 J. Xu, X. Sun, B. Sun, H. Zhu, X. Fan, Q. Guo, Y. Li, Z. Zhu and K. Qian, *ACS Appl. Mater. Interfaces*, 2023, **15**, 33774–33783.
29 H. Xiao, S. Li, Z. He, Y. Wu, Z. Gao, C. Hu, S. Hu, S. Wang, C. Liu, J. Shang, M. Liao, D. Makarov, Y. Liu and R. Li, *Adv. Funct. Mater.*, 2023, **33**, 2214907.
30 M. Jung, J. Lee, S. K. Vishwanath, O.-S. Kwon, C. W. Ahn, K. Shin and S. Jeon, *Flex. Print. Electron.*, 2020, **5**, 025003.
31 Z. Wu, W. Shi, H. Ding, B. Zhong, W. Huang, Y. Zhou, X. Gui, X. Xie and J. Wu, *J. Mater. Chem. C*, 2021, **9**, 13668–13679.
32 J. Zhang, W. Xue, Y. Dai, C. Wu, B. Li, X. Guo, B. Liao and W. Zeng, *Composites, Part A*, 2023, **171**, 107572.
33 F. Li, Y. Liu, X. Shi, H. Li, C. Wang, Q. Zhang, R. Ma and J. Liang, *Nano Lett.*, 2020, **20**, 6176–6184.
34 Y. Zhang, W. Jie, P. Chen, W. Liu and J. Hao, *Adv. Mater.*, 2018, **30**, 1707007.
35 L. Lai, W. Zeng, X. Fu, R. Sun and R. Du, *Surf. Coat. Technol.*, 2013, **218**, 80–86.
36 L. Lai, X. Fu, R. Sun and R. Du, *Surf. Coat. Technol.*, 2013, **235**, 552–560.
37 I. H. Kazi, P. M. Wild, T. N. Moore and M. Sayer, *Thin Solid Films*, 2003, **433**, 337–343.
38 A. DeHennis and K. D. Wise, in TRANSDUCERS '03. 12th International Conference on Solid-State Sensors, Actuators and Microsystems. Digest of Technical Papers (Cat. No. 03TH8664), IEEE, Boston, MA, USA, 2003, **2**, 1860–1863.
39 A. D. DeHennis and K. D. Wise, *J. Microelectromech. Syst.*, 2005, **14**, 12–22.
40 H.-Y. Ma, Q.-A. Huang, M. Qin and T. Lu, in 2009 IEEE Sensors, IEEE, Christchurch, New Zealand, 2009, 1693–1696.
41 C.-H. Cai, M. Qin and J.-Q. Huang, in 2012 IEEE Sensors, IEEE, Taipei, Taiwan, 2012, 1–4.
42 Q.-Y. Ren, L.-F. Wang and Q.-A. Huang, *Electron. Lett.*, 2016, **52**, 1345–1347.
43 U. Salmaz, T. Islam and S. Sohail, *IEEE Trans. Instrum. Meas.*, 2020, **69**, 7887–7894.
44 J. Ji, C. Zhang, S. Yang, Y. Liu, J. Wang and Z. Shi, *ACS Appl. Mater. Interfaces*, 2022, **14**, 24059–24066.
45 Y. Zheng, Y. Li, Y. Zhou, K. Dai, G. Zheng, B. Zhang, C. Liu and C. Shen, *ACS Appl. Mater. Interfaces*, 2020, **12**, 1474–1485.
46 Y. Bu, T. Shen, W. Yang, S. Yang, Y. Zhao, H. Liu, Y. Zheng, C. Liu and C. Shen, *Sci. Bull.*, 2021, **66**, 1849–1857.
47 K. Zhai, H. Wang, Q. Ding, Z. Wu, M. Ding, K. Tao, B. Yang, X. Xie, C. Li and J. Wu, *Adv. Sci.*, 2023, **10**, 2205632.
48 Y. Yang, L. Shi, Z. Cao, R. Wang and J. Sun, *Adv. Funct. Mater.*, 2019, **29**, 1807882.
49 J. Li, R. Bao, J. Tao, M. Dong, Y. Zhang, S. Fu, D. Peng and C. Pan, *Appl. Phys. Rev.*, 2020, **7**, 011404.
50 Y. Lu, D. Zhao, J. He, L. Zou, J. Wang and S. Song, *J. Mater. Chem. A*, 2022, **10**, 22551–22560.
51 Y. Zhou, Y. Wu, W. Asghar, J. Ding, X. Su, S. Li, F. Li, Z. Yu, J. Shang, Y. Liu and R.-W. Li, *ACS Appl. Electron. Mater.*, 2019, **1**, 1866–1872.

